Hot carrier photocatalysis using bimetallic Au@Pt hemispherical core–shell nanoislands

Manuel, Ajay P.; Riddell, Saralyn; Rajashekhar, Harshitha; Vrushabendrakumar, Damini; Alam, Kazi M.; Kumar, Pawan; Gusarov, Sergey; Kobryn, Alexander E.; Supur, Mustafa; McCreery, Richard L.; Shankar, Karthik

Publisher's version / Version de l'éditeur:
https://doi.org/10.1007/s10854-022-08671-2
Journal of Materials Science: Materials in Electronics, 33, 22, pp. 18134-18155, 2022-07-11

Hot Carrier Photocatalysis Using Bimetallic Au@Pt Hemispherical Core-Shell Nanoislands

Ajay P. Manuel,[1] Saralyn Riddell,[1] Harshitha Rajashekhar,[1] Damini Vrushabendrakumar,[1] Kazi Alam,[1,2] Pawan Kumar,[1†] Sergey Gusarov,[2] Alex Kobryn,[2] Mustafa Supur,[3] Rick McCreery,[3] Karthik Shankar[1]*

[1] Department of Electrical and Computer Engineering, University of Alberta, Edmonton, AB, Canada, T6G 1H9

[2] Nanotechnology Research Center, National Research Council Canada, 11421 Saskatchewan Drive, Edmonton, AB, Canada, T6G 2M9

[3] Department of Chemistry, University of Alberta, Edmonton, AB, Canada, T6G 2G2

†Current Address: *Department of Chemical and Petroleum Engineering, University of Calgary, 2500 University Drive, NW Calgary, Alberta, Canada*

* Email: kshankar@ualberta.ca

Keywords: plasmonic catalysis, dye degradation, methylene blue, hot-electron mediated photocatalysis, Raman thermometry, surface enhanced Raman scattering.

Abstract: We report the fabrication of core-shell Au@Pt nanoislands grown on glass substrates using a facile and reproducible combination of magnetron sputtering and thermal annealing. Au@Pt NPs exhibit a lattice strain of ~0.2% and a slightly positively charged Au core due to electron transfer from Au to Pt during equilibration. The localized surface plasmon resonance peak of Au redshifts incrementally from 2.13 to 2.0 eV and broadens in a controllable manner with the addition of ultrathin Pt shells (1-3 nm). The quality factor of the LSPR resonance decreased gradually from ~13 to ~3 as bare Au nanoislands were coated with 3 nm of Pt. The Au@Pt nanoislands demonstrated superior methylene blue degradation performance due to the hot hole injection from the bimetallic nanoparticle into the dye molecule despite the absence of any semiconducting photocatalytic support. Raman thermometry studies involving Stokes and anti-Stokes spectra helped shed light on the hot electron dynamics of the composite system and validates hot carrier injection from Au to Pt.

1. Introduction

Plasmonic photocatalysis has recently emerged as a promising pathway for promoting chemical reactions through the excitation of collective charge density oscillations in coinage metal nanoparticles (NPs).[1-4] Au NPs interact strongly with incident electromagnetic radiation due to the localized surface plasmon resonance (LSPR) phenomena resulting in enhanced absorption and the ability to harvest light in nanoscale volumes.[5-9] The LSPR excitation can dephase radiatively through the emission of a photon or non-radiatively through the generation of a transient population of non-equilibrium excited charge carriers or hot electrons.[10] These photoexcited electrons can be transferred directly to adsorbed reactant molecules or elevate the temperature of the nanoparticle by releasing their energy in the form of heat.[11-13] Enhanced photothermal effects increase the overall kinetics of chemical reactions. Increased photonic radiation helps enhance local chemical reactions such as photodegradation, photoisomerization, and light collection.[11, 14] Hot electrons promote metal-adsorbate systems to an excited state effectively allowing for lowered activation energy barriers.[12, 15] Thus, plasmonic noble metal NP photocatalysts can be utilized to exploit and increase the reaction rates and product selectivity of numerous industrially- and environmentally-relevant reactions under relatively mild conditions.[3, 11, 16-25]

Traditional plasmonic noble metals such as Au, Ag, Cu, etc. are highly attractive as their LSPR peaks can be tuned throughout the visible to near-infrared spectrum where solar irradiation is strongest by modifying the morphology, size, and dielectric environment of the nanoparticles.[1, 26, 27] The primary limitation of Au NPs for catalysis is their inherent inertness. Bimetallic nanoparticles offer a solution to this problem whereby the combination of Au with catalytic transition metals such as Pt, Pd, Rh, Ru, etc. forms an ideal photocatalyst with optical properties of the plasmonic metal and the reactive properties of the catalytic metal. These bimetallic nanostructures are largely fabricated in the form of antenna-reactor,[28, 29] core-shell,[1, 30-33] or alloy structures,[34-36] and compared to their monometallic counterparts have demonstrated greater optical sensitivity,[17, 19] product selectivity,[28, 37] and increased reaction rates[38-41] for diverse chemical reactions.[11] Unlike metal-semiconductor heterojunction systems, bimetallic nanostructures come with the added benefit of facilitating enhanced charge carrier separation while omitting the need for a semiconductor heterojunction.[42, 43] Herein, we investigate the fundamental behavior of Au@Pt core-shell nanoislands in plasmonic photocatalysis using a combination of density functional theory computations, Raman thermometry, photoelectron spectroscopy and photocatalytic activity evaluation in the presence of radical scavengers. Catalytic metals such as

Pt have a weak optical response in the visible, and strongly absorb UV photons. The addition of an Au core as a plasmonic antenna and thin shells of Pt as catalytic layers are used to create a bimetallic photocatalyst retaining the optical behavior of the plasmonic metal and reactive behavior of the catalytic metal for catalytic applications beyond the boundaries of its constituents.[1, 15, 44]

A combination of magnetron sputtering, and thermal annealing is used to form hemispherical Au@Pt core-shell nanoislands on glass substrates in a facile process that is less time-consuming while providing greater consistency compared to wet-chemical or colloidal synthetic techniques.[45] The addition of ultrathin Pt shells for varying durations of deposition provides insights in modulating the plasmonic behavior of the core-shell composite and is observed to directly influence the use of these plasmonic substrates for efficient degradation of methylene blue (MB). Stokes and anti-Stokes surface-enhanced Raman scattering (SERS) intensities of the bimetallic-adsorbate system clarify the microscopic mechanism of the excitation and the flow of energetic charge carriers in a Dissociated Induced Electron Transfer (DIET) process between the plasmonic and adsorbate systems.[46, 47] This analysis provides us a direction of control of the charge excitation and transfer process that may be explored using interfacial and local electric field engineering

strategies. Preliminary knowledge on the plasmonic substrates has been obtained by considering finite-difference time-domain (FDTD) simulations on the electromagnetic response characteristics and the influence of morphology on the overall behavior of the macroscale structure. Density functional theory simulations have also been utilized to explore the influence of chemical and interfacial characteristics of the Au@Pt core-shell substrates. Although it is favorable to provide for semiconducting scaffolds in conjunction with plasmonic substrates, these studies, overall, demonstrate the versatility of the method utilized to synthesize these bimetallic structures, their potential as standalone nanostructures for plasmon-driven catalytic reactions and chemical conversion, all the while permitting facile incorporation in semiconductor scaffolds.[45, 46, 48]

2. Results and Discussion

2.1 Morphological and compositional studies of Au@Pt core-shell nanoislands

A combination of magnetron sputtering, and thermal annealing was used to fabricate bimetallic Au@Pt core-shell nanoislands (see the Materials and Methods section in the Supporting Information). Figure 1a presents a FESEM image of Au@Pt films annealed at 400 °C. Annealing of the Au films induces thermal dewetting allowing Au atoms at the surface to migrate and form individual nanoislands. Figure 1a shows that the Au film annealed at 400 °C generally exhibits a

hemispherical morphology while maintaining a non-uniform size distribution. These observations are similar to those from monometallic Ag nanoislands fabricated with the same procedure.[39] Deviations are observed where particles are elongated and oblate in shape as opposed to spherical. The average nanoisland size with the error was determined to be ~ 80 ± 25 nm and a polydispersity of ~ 30% (Figure S1). The size distribution is monomodal in nature, a behavior that can be attributed to the temperature at which the bimetallic substrates are treated (similar to what was observed for monometallic Ag nanoislands) and which satisfies the condition of dewetting as required by the H*ü*ttig and Tammann limits for Au (whose melting point is 1064 °C).[49, 50] This dependence of dewetting behavior with annealing temperature was also observed in the work of Kracker et al.[51] who recognize that at higher temperatures Au particles become uniformly rounded leading to a monomodal size distribution. This is also supported by the work of Müller et al.[52] where only dewetted Au layers with a thickness of more than 10 nm showed bimodal size distributions. Our magnetron sputtering system, utilized to fabricate these islands, registers an average deposition rate of 7.6 nm/min for Au. 40 s of deposition of Au films corresponds to a 5 nm thick film. The glass substrate was not damaged during thermal treatment and the dewetting process was largely governed by the minimization of the surface energy of the deposited metal

film.[45] The morphological changes observed for Au films are similar to the general conditions of thin-film growth which involves adsorption, cluster formation, surface diffusion, desorption, nucleation, island growth, and agglomeration, all of which were observed in our sputtered and annealed Au films.[53] By changing the duration of annealing at a given temperature, the extent of particle agglomeration can be monitored.[45] Following the annealing of the Au films, Pt thin films were sputtered for varying durations between 10 – 30 s to form conformal shells coating the Au nanoislands. Due to the thin nature of the films, the presence of Pt is difficult to discern *via* FESEM. However, the presence of the Pt shell layer in the Au-Pt composite was confirmed via XPS studies.

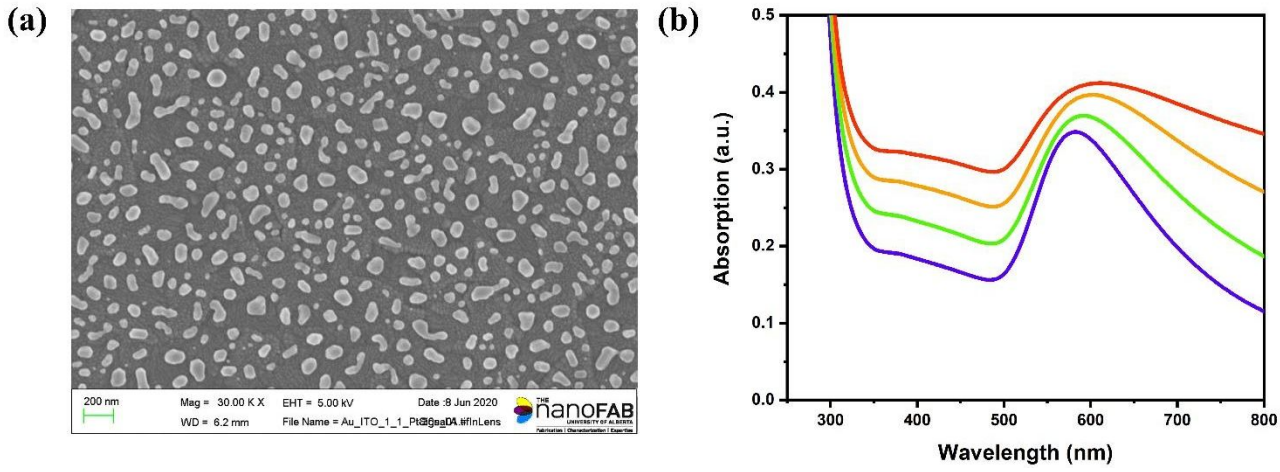

Figure 1. (a) FESEM image of Au@Pt hemispherical core-shell nanoislands formed on a glass substrate. (b) UV-Vis absorbance spectra of monometallic Au film on glass annealed at 400 °C (violet), and post Pt depositions of 10 s (green), 20 s (orange), and 30 s (red).

The surface and sub-surface (up to ~10 nm) chemical composition of samples was determined by measuring the binding energies using X-ray photoelectron spectroscopy (XPS) (Figures 2a,c-d). Survey scan XPS spectra (see the Materials and Methods section in the Supporting Information) of monometallic Au and Pt samples, as well as bimetallic Au@Pt samples, displayed all the core level (Au4f, Pt4f) and sub-core-level peaks (Au3d, Au3p, Pt3d and Pt3p) confirming the presence of the constituent elements (Figure 2b). Deconvoluted high-resolution XPS spectra of Au in Au4f region show two well-resolved peaks at binding energies (BE) 83.6 and 87.3 eV assigned to $Au4f_{7/2}$ and $Au4f_{5/2}$ peak components of metallic Au in zero oxidation state. The absence of any additional peak or shoulder peak excludes the possibility of oxidation during sputtering.

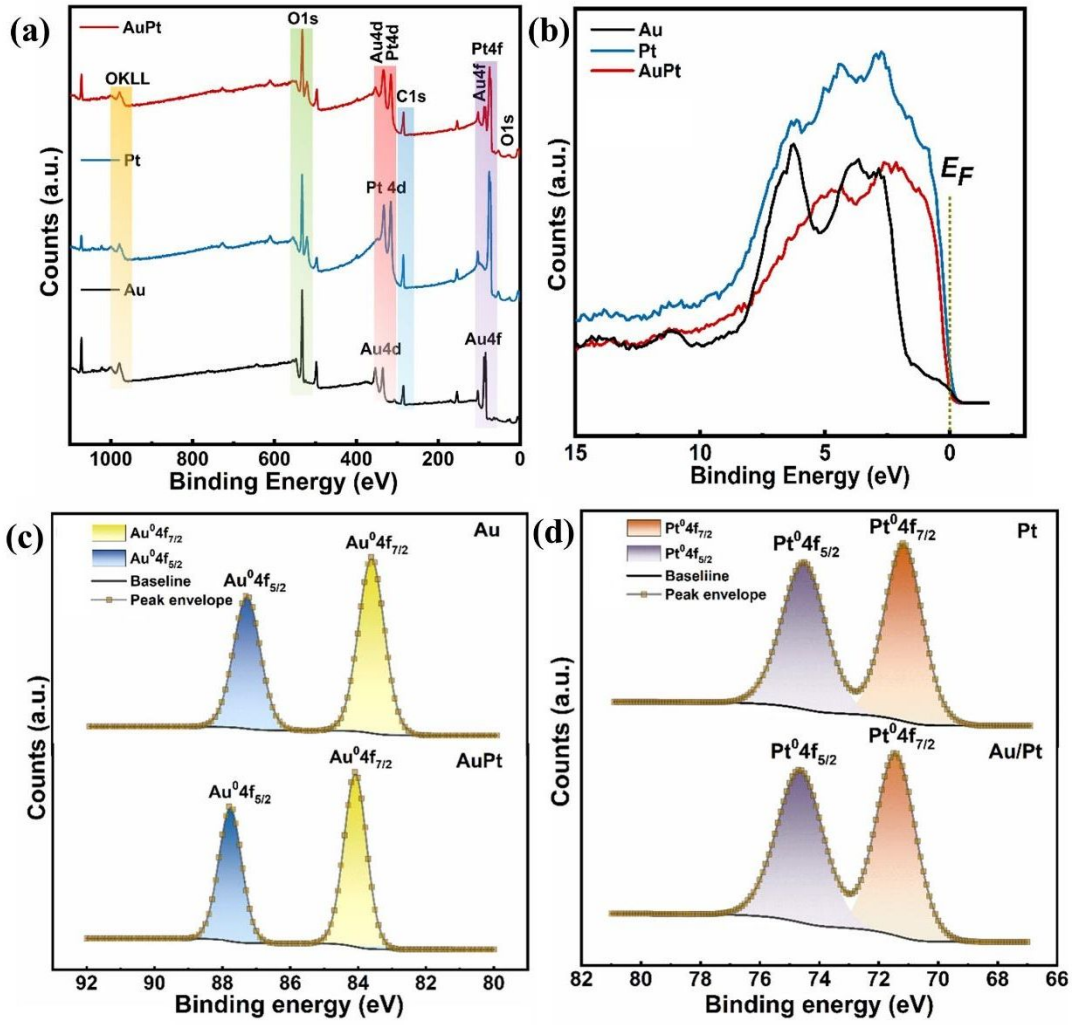

Figure 2. (a) Survey scan XPS spectra of monometallic Au, Pt and bimetallic Au@Pt samples that confirm the presence of the constituent elements. (b) XPS valence band spectra of Au, Pt and Au@Pt (c)-(d) Binding energies of the Au and Pt constituents in the monometallic and bimetallic counterparts.

Following the formation of Au@Pt core-shell structures, the BE of Au was slightly shifted toward higher energies and new peaks were observed at 84.1 and 87.8 eV. The positive shift in the binding energy value of Au in the core-shell bimetallic NP suggests the transfer of electrons from

the Au core to the Pt shell. As the Fermi level of Pt is lower than Au, the electrons in an Au@Pt bimetallic system will flow from Au to Pt due to the built-in electric field until Fermi level equilibration. This electron transfer leads to decreased electron density (increased positive charge) on Au resulting in a positive shift in BE. Furthermore, increased BE also exclude the possibility of Au@Pt alloy formation, as in alloys the higher electronegativity of Au (2.54) than Pt (2.2) and perturbed electronic interaction between Pt and Au atomic orbitals would lead to charges being transferred from Pt to Au while the opposite has been observed here.[36] It is critical to note that under LSPR excitation, the slight positive charge in the gold core of the Au@Pt bimetallic nanoparticles would cause hot electrons to be retained in the Au core and hot holes to be transferred to Pt.

The appearance of two well-resolved peak components at 71.2 and 74.5 eV in Pt4f XPS of Pt metal, assigned to $Pt4f_{7/2}$ and $Pt4f_{5/2}$ orbital splitting, validates the presence of Pt in its metallic state. Contrary to prediction, no negative peak shift in the BE value of Pt was observed in the Au@Pt core-shell structure. This could be due to the accumulation of electrons at the Au@Pt interface or the deactivation of surface electrons via O_2 which works as an electron scavenger. XPS valence band spectra of Au show a characteristic doublet of 5d band with a d band edge at ~2

eV below the Fermi level while the 6s band edge as free electrons were observed at zero binding energy. For Pt, the 5d band was observed at the Fermi level.[54, 55] These observations match multiple studies of Au@Pt systems where the core-shell structure is often characterized by a positive shift in BE for Au and a mostly unchanged Pt BE in the XPS spectra. Interestingly, the valence band spectra of Au@Pt follow a similar pattern as of Pt suggesting the coverage of Au core with Pt shell. Slight energy variation (-0.1 to -0.2 eV) was attributed to charging or insufficient grounding of the glass substrate. Tan et al.[56] utilize the corresponding shifts in binding energies of the Au 4f and Pt 4f orbitals to confirm the charge transfer phenomenon in their Au@Pt bimetallic structure. Wang et al.[54] demonstrate large numbers of Au bimetallic systems where electropositive hosts, such as Pt, may often result in a positive BE shift in the Au 4f levels, which is also observed in our work. Bond et al.[57] further argue that the Au-Pt phase diagram exhibits a considerable miscibility gap meaning the solubility of each metal in the other is strictly limited. Atomistic calculations and thermodynamic studies of nanoalloys as demonstrated Wang et al.[58] suggest the possibility of a core-shell structure as opposed to an Au-Pt alloy considering the low temperatures and low Pt amounts involved.

Ultraviolet photoelectron spectroscopy (UPS) was used to determine the work function for Au, Pt, and Au@Pt core-shell nanoisland substrates (Figures S3 – S5).[59] To calculate the work function, the formula $WF(\phi) = 21.21 - E_{cut\text{-}off}$ was utilized, where 21.21 eV refers to the energy of the incident He-I line of the He discharge lamp, and $E_{cut\text{-}off}$ is the cut-off energy of secondary electrons. The point of intersection of the leading edge of the graph provides the value for $E_{cut\text{-}off}$ and is determined via extrapolation. The value of $E_{cut\text{-}off}$ for Au, Pt, and Au@Pt samples was found to be 16.5 eV, 16.7 eV, and 16.07 eV, respectively, corresponding to work function values of 4.71 eV, 4.51 eV, and 5.14 eV, respectively (Figures S2-S4). The secondary electron cut-off for Au@Pt is noticeably shifted toward lower energies compared to its monometallic components. The work function of Au is observed to be well within the range of values commonly reported for gold while the low work function of Pt could be attributed to the incomplete development of metallicity due to the low thicknesses of the deposited film. It can also be argued that due to electron transfer from the Au to the Pt shell, the surface is electron-rich, resulting in Fermi level shifting of Pt. As UPS WF spectra and XPS VB spectra use low-energy photons, we are considering information at the surface of Pt, evident from the similarity index of XPS valence band spectra of Au@Pt and Pt. Since Pt is also exposed to air and moisture alongside its high surface energy, there is the possible coverage of the Pt surface with weakly bonded O_2/H_2O as well.

XRD studies (Figure S2) demonstrate that the sputtered bare Au and Pt films display crystal planes of the typical face-centered-cubic (fcc) phase of Au[60] (JCPDS no. 04-0784) and fcc phase of Pt[61] (JCPDS no. 04-0802). Table 1 lists the crystallite sizes and microstrains of pristine Au, Pt, and Au@Pt substrates.

	Average crystallite size (nm)				**Microstrain (10^{-3})**			
	hkl (111)	*hkl* (200)	*hkl* (220)	*hkl* (311)	*hkl* (111)	*hkl* (200)	*hkl* (220)	*hkl* (311)
Au	5.54	5.06	5.37	6.53	19.1	18.2	11.8	8.5
Au@Pt	5.40	5.31	5.31	6.57	19.6	17.3	11.9	8.4
Pt	4.7	5.96	5.63		21.7	14.9	11.1	

Table 1. Average crystallite size and microstrain values for pristine Au, Pt, and Au@Pt substrates extracted from XRD peak widths in (Figure S2).

The incorporation of Pt upon Au nanoislands does not result in a significant change in crystal size. Indeed, it can be observed that the average crystallite size is largely consistent among the monometallic constituents and the bimetallic composites for the various crystal planes. While 5 nm is a small value for the average crystallite size, metallicity is generally expected to manifest around this landmark. Vacuum deposition usually results in polycrystalline films, unlike colloidal methods where one obtains monocrystalline films. As demonstrated by Goubet et al.[62] and Staechelin et al.[63] for the similar crystallite sizes calculated, the broadening of the peaks observed

in the LSPR spectra (an increase in linewidth) can be attributed to faster electron-phonon coupling, which reduces the thermal equilibrium time of hot carriers, and surface scattering of electrons on defects and grain boundaries. Strain in Au films is generally expected as thermal dewetting implies inefficient lattice matching due to Au's poor adsorption onto a glass substrate. Strain magnitudes for the Pt films are generally around the same magnitude except for the (111) direction where there is a near 10% increase. Between the two metal constituents, Au is known to have a larger lattice constant than Pt. Thus, the latter is subject mainly to tensile while Au would be under compressive strain.[64] It is observed that there is a lattice strain accumulation largely at (111) planes followed by a lattice relaxation effect acting upon the remaining crystal planes in (200), (220), and (311). This leads us to conclude that any expected tensile strain in the bimetallic substrates is released through the formation of lattice defects in the form of distortions or dislocations on (111) planes.[64]

2.2 LSPR modulation in bimetallic Au@Pt nanoislands

Figure 1b presents the UV-Vis-NIR spectra of monometallic Au nanoislands (violet) and bimetallic Au@Pt core-shell nanoislands (green, orange, red) (see Supporting Information). The bimetallic nanoislands are fabricated with varying thicknesses of Pt shells evidenced via differing magnetron sputtering deposition times between 10 – 30 s. In Au films annealed at 400 °C, the

primary dipolar plasmon resonance of the nanoislands is observed at a wavelength of 582 nm. This can be because the incident electric field of light is uniform over the entire volume of the Au nanoparticle.[65] The hemispherical shape and the high index glass substrate ($\epsilon = 1.5$) are responsible for the red-shifted plasmon resonance of the Au nanoislands. The redshifted values of the plasmon resonance and the clear broadening of the primary resonance peak are a consequence of the high annealing temperature utilized. They are indicative of the average particle size due to thermal dewetting of the gold nuclei, and subsequent coalescence of individual smaller particles to nearby larger particles via surface diffusion and mass transfer. The resultant morphology of the Au nanoislands thus matches what is expected by the Young-Dupre equation for particle sizes > 100 nm.[66] The absence of quadrupole resonances in the short-wavelength spectral region for these Au nanoislands agrees with what has been observed in the literature.[67, 68]

Adding Pt catalytic shells onto the Au nanoislands results in the damping of the plasmon resonance that was directly observed from the absorption spectra (Figure 1b). For increasing sputtering deposition times of 10 s (green; LSPR peak at 592 nm), 20 s (orange; LSPR peak at 603 nm), and 30 s (red; LSPR peak at 614nm) the plasmon resonance of Au@Pt core-shell nanoislands experience a damping of the plasmon resonance observed as a collectively broadening of the LSPR

resonance peak, and further red-shifting of the peak. The increase in absorption magnitude follows the rising trend of greater thicknesses of Pt shells being deposited atop the Au nanoisland. The evolution of the quality factor (Q) of the plasmon resonances, the ratio of the peak plasmon resonance frequency and the FWHM or ω_{peak}/FWHM, also demonstrates the progression of damping with ~ 4.64, 3.50, 2.54, and 2.49 from the bare Au sample and to those post-deposition with Pt for 10 s, 20 s, and 30 s, respectively. The quality factor can also be used as a key metric to evaluate plasmonic substrates as the resultant local electromagnetic field enhancement and plasmon dephasing times due to the LSPR are directly proportional to Q.[69] The Q values calculated from the UV-Vis spectra also provide information about the ensembled averaged enhancement factors.[70]

This overall behavior is unique as compared to what has been generally observed in bimetallic substrates involving Au and Pt where the dampening of the plasmonic response is usually observed with the LSPR blue shifting in energy and losing intensity.[11, 32, 71] The broadening of the resonance in spectral shape does concur with the consensus that intermetallic effects between the plasmonic noble metal and catalytic transition metal can lead to optical and catalytic behavior distinct from the sum of their parts.[1, 11, 15, 71] As the plasmon resonance itself is highly dependent on the

morphology of the nanoparticle, these observations may differ between core-shell nanostructures of varying morphology.

The origin of this behavior can also be traced to the electronic band structures of plasmonic and catalytic metals. It is well-known that the d-band for plasmonic metals is far from the Fermi level. This allows for high-quality, intraband plasmons (s to s) at optical frequencies until the onset of interband transitions (d to s). In contrast, catalytic metals have d-band centers close to the Fermi level resulting in their optical responses being dominated by interband transitions. Thus, there is an increased probability of interband transitions that dampens the LSPR at all frequencies resulting in a broadening of the resonance peak.[11, 32, 54]

For Au@Pt bimetallic substrates, the constituent LSPRs of Au and Pt are highly nondegenerate due to differences in free carrier density and the effective masses of the two materials. Thus, the Au electrons do not oscillate in resonance with Pt electrons, and therefore, both components contribute very little to the other's LSPR.[1, 72, 73] It has been experimentally demonstrated that a single monolayer of Pt on an Au core leads to a dramatic drop of ~ 90% in absorption intensity.[73] This has also been recognized in studies on other bimetallic systems.[1, 32, 74-77]

The facile means of fabrication and the subsequent modulation of the plasmon resonance by varying the thickness of the catalytic metal shell provide an important design parameter for optimizing the performance of bimetallic core-shell photocatalysts. FDTD electromagnetic simulations provide additional insights into this behavior as well as help to demonstrate the mechanisms of plasmon modulation due to the addition of a catalytic shell and the corresponding local electric field enhancement behavior.

2.3 FDTD studies of LSPR modulation in Au@Pt substrates

Using Mie theory, Zhang et al. found that spherical core-shell structures support two types of plasmon resonances: ordinary and extraordinary modes.[32] The energy of the ordinary mode is concentrated at the outer surface of the shell while the energy of the extraordinary mode is concentrated at the interface between the core and the shell. This is similar to bonding and antibonding modes in plasmon hybridization though this is not evident in all systems in the visible range.[78, 79] The LSPR peak of bimetallic systems thus will be redshifted or blue-shifted depending on the type of mode or the effective permittivity of the shell.

Various FDTD simulations on glass substrates were performed with results involving Au nanoislands of radii 30 nm matching best with a dipole resonance peak value at 584 nm (see

Supporting Information). It was observed that for an array of Au nanoislands conformally coated with Pt shells of varying thicknesses ranging from 1 nm – 3 nm the general trend in bimetallic spectra was observed (Figure 3b). As shown in Zhang et al.,[28] the plasmon resonance is an ordinary LSPR mode that experiences a loss in intensity, broadens in spectral shape, and blue-shifts as the thickness of the catalytic Pt shell increases.

The local electric fields are concentrated at the air/Pt interface which is induced by the metallic features of Pt the visible wavelength (Figures 3c,d). By modulation of the thickness of the Pt shell, it is observed that the local electric field gets weaker for thicker Pt shells as observed in (Figures 3c,d) where Pt shell thickness increase from 1 nm to 3 nm. The amplification of the local field for thinner shells is beneficial for photocatalysis and is in accord with the results presented by the work of Engelbrekt et al.[1] These observations also agree with other existing literature.[11, 15, 32, 71]

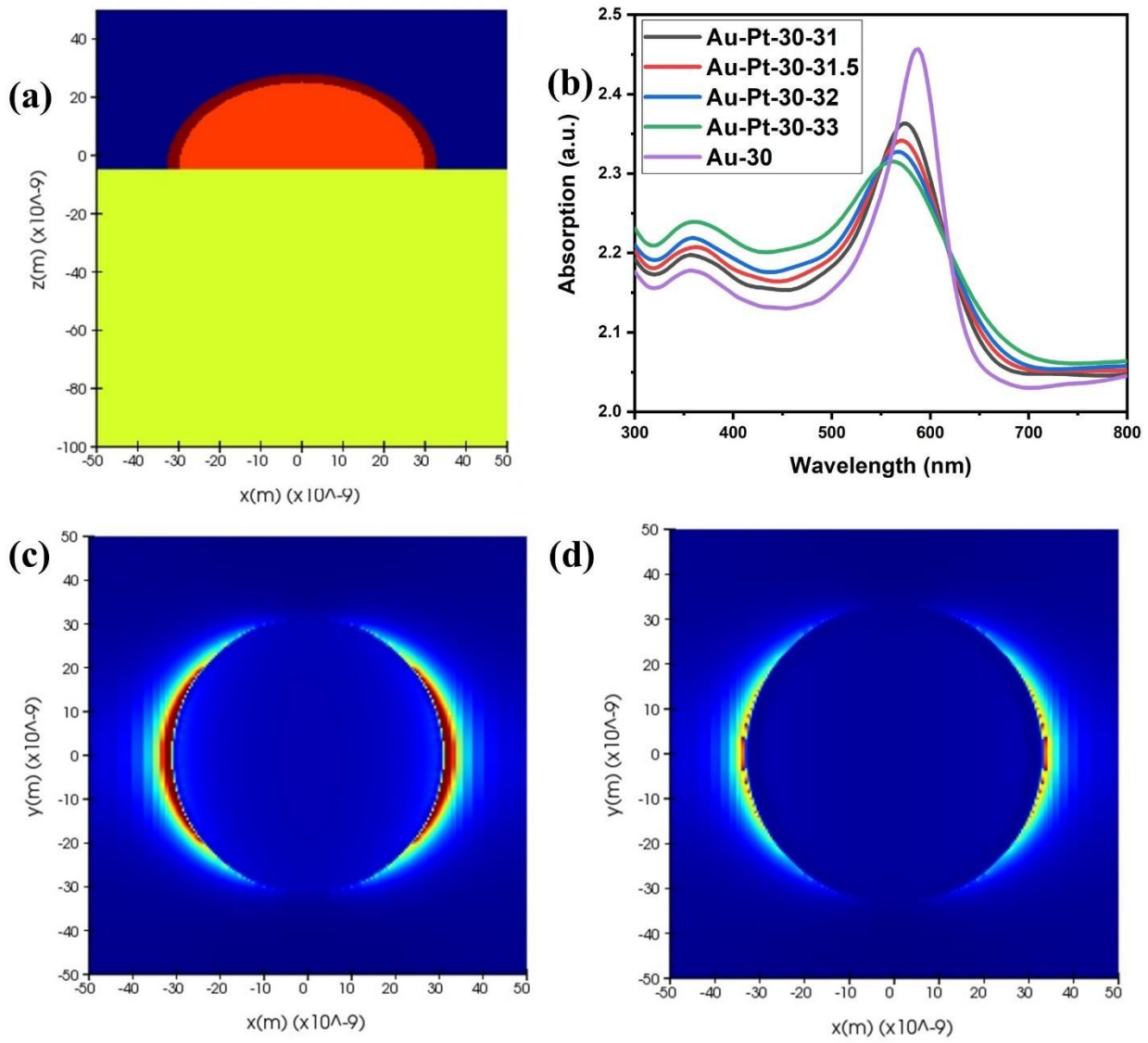

Figure 3. (a) Index monitor profile of the Au@Pt bimetallic hemispherical nanoisland core-shell structure. (b) Absorption spectra of Au@Pt bimetallic core-shell structure with an Au core radius of 30 nm and Pt shell thicknesses from 1 – 3 nm. The characteristics ratios of these radii are presented in the legend as 30 – 31 nm, 30 – 31.5 nm, etc. (c) Electric field profile intensity graph of Au@Pt core-shell structure with a core radius of 30 nm and a shell thickness of 1 nm. (d) Electric field profile intensity graph of Au@Pt core-shell structure (along the xy-plane) with a core radius of 30 nm and a shell thickness of 3 nm.

Figure 1b confirms there is a significant difference in morphology that justifies unique resonances observed in our Au@Pt substrates compared to these general trends. Following thermal treatment of Au films, Pt films are deposited along the entire surface of the glass substrate. Thus, unlike earlier simulations of individual hemispherical core-shell nanoislands, FDTD simulations of Au nanoislands with Pt shells that conformally coated both the plasmonic core as well as the glass substrate were investigated. The corresponding results (Figure 4) match experimental observations and confirm the morphology of our Au@Pt substrates. Upon addition of Pt shells, the corresponding broadening and redshift of the primary plasmon resonance of Au is observed (Figure 4b). The subsequent redshift can be attributed to the morphological and structural characteristics of the Au@Pt substrates. Unlike isolated bimetallic Au@Pt nanoparticles, the nanostructured films consist of hemispherical Au nanoislands separated from each other by inter-island channels. The width of these inter-island channels can be modulated by changing the duration and temperature of the annealing process with narrower channels generally being observed for lower temperatures and shorter durations.[45, 53, 80] The shifts in resonance observed can also arise due to charge transfer and may vary for asymmetric particles.[32] As before, the electric

field density profiles follow the trend where for increasing Pt shell thickness the plasmon resonance is damped. But unlike earlier, the presence of a thin Pt layer surrounding the bimetallic nanoisland results in the generation of a more intense local electric field around the vicinity of the nanostructure. The generation of a stronger local electric field correlates to a stronger plasmon resonance while the Pt film serves as an offsite catalytic surface and as a protective insulating layer for the plasmonic noble metal Au core. As demonstrated by Huang et al.[17] the presence of Pt as a conform shell on the Au nanoisland and surrounding its vicinity helps increase the ratio of light absorption to scattering due to Pt's large imaginary dielectric permittivity at visible and near-infrared frequencies. This is attributed to Pt's high density of d-states at the Fermi level and strong sp<-d interband transitions.[17] Together, the combination of a large imaginary dielectric permittivity and high plasmonic field intensity results in strong light absorption in the shell, and helping transfer light energy from the core to the surface. This is beneficial for the plasmonic enhancement of molecular adsorption and chemical reactivity.

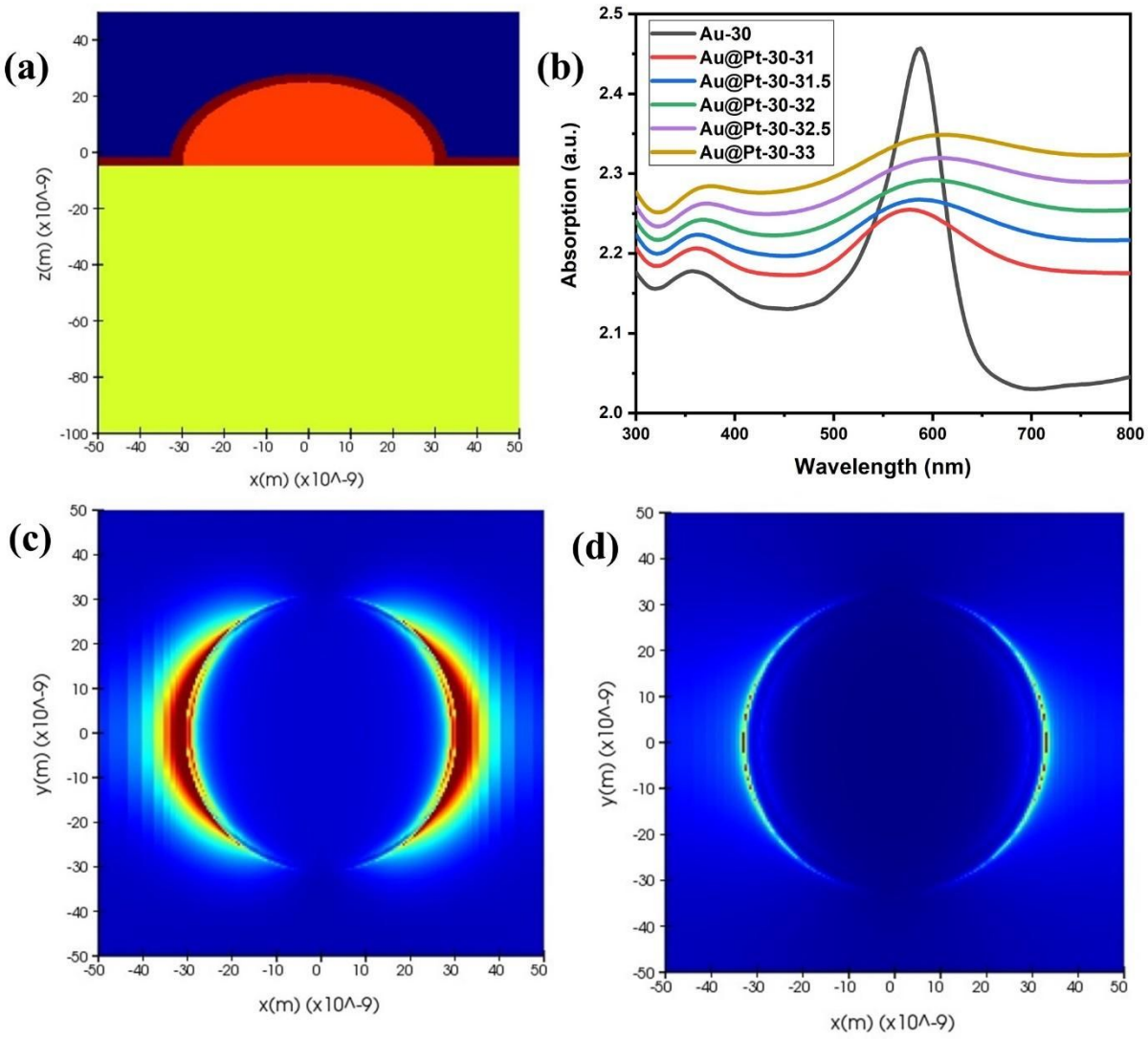

Figure 4. (a) Index monitor profile of the Au@Pt bimetallic hemispherical nanoisland core-shell structure with a thin film of Pt on the glass substrate as well. (b) Absorption spectra of Au@Pt bimetallic core-shell structure with an Au core radius of 30 nm and Pt shell thicknesses from 1 – 3 nm. The characteristics ratios of these radii are presented in the legend as 30 – 31 nm, 30 – 31.5 nm, etc. (c) Electric field profile intensity graph of Au@Pt core-shell structure with a core radius of 30 nm and a shell thickness of 1 nm. (d) Electric field profile intensity

graph of Au@Pt core-shell structure (along the xy-plane) with a core radius of 30 nm and a shell thickness of 3 nm.

As observed by Agarwal et al.[48], the existence of inter-island channels between Au nanoislands provide additional amplification of the localized electromagnetic field, with the highest enhancements occurring at the channel-shaped gaps between adjacent islands. These intense local electric fields generated by these structures can be used to trigger chemical reactions[81] and also work as in situ probes to deduce the reaction mechanism via surface enhanced Raman spectroscopy (SERS).[82, 83] The deposition of Pt in these areas provides for an effective composite bimetallic photocatalyst. The facile means of fabrication of these bimetallic substrates and the modulation of their plasmon resonance characteristics for broad optical absorption make them viable for visible light photocatalytic and plasmon-driven chemical reactions.

The preliminary UV-Vis-NIR spectra now supplemented by electromagnetic FDTD analyses demonstrate the potential of Au@Pt core-shell nanoislands as standalone substrates for plasmon-enhanced photocatalysis (Figure 4). The resultant LSPR peaks observed in the simulations and experiments are beneficial for photocatalytic applications where one tries to match the broad solar spectrum. All the simulations discussed above involved arrays of hemispherical bimetallic

nanoislands structured with a center-to-center spacing of 100 nm indicating that there is a negligible role of Coulombic interactions from neighboring particles.[45]

2.4 Density Functional Theory studies

The intermetallic effects of bimetallic core-shell nanostructures are heavily influenced by the geometry of the bimetallic structure and can potentially provide information on optical coupling via plasmon hybridization, electronic coupling via charge transfer, and possibly even atomic coupling via the formation of a new electronic structure.[11] Density functional theory (DFT) based quantum chemical calculations were pursued to garner valuable insights into the electronic structure of the bimetallic system (see Supporting Information). Figure 5 displays the first, second and third highest occupied molecular orbital (HOMO) and lowest unoccupied molecular orbital (LUMO) when Au (111) and Pt (111) are far away from each other and when Au (111) and Pt (111) are in close configuration. The highest occupied and lowest unoccupied molecular orbitals are positioned predominantly on Au and Pt clusters respectively in close configuration. Such molecular orbital locations suggest a possible charge transfer phenomenon from gold to platinum under illumination. Figures 6a and b show the average projected density of states (PDOS) of Pt and Au systems for Au (111) and Pt (111) hybrid systems in far and close configurations,

respectively. The density of states refers to the number of different states at a particular energy level that electrons can occupy. The PDOS is the relative contribution an atom or orbital makes to the total density of states. It is analogous to the Aufbau principle but generalized to larger molecular systems. The PDOS plots show discrete energy levels or narrow bands akin to molecules as opposed to the broad bands expected in real metals. The average PDOS was obtained by averaging over all the DOS projected on individual atomic sites. Figures 6c,d show the orbital-resolved PDOS of selected Pt and Au atoms at the interfacial region in the far configuration, which show the relative contribution of different orbitals to the occupied and unoccupied regions of the metallic systems under study.[84, 85] Note that these plots are generated for Au and Pt clusters containing only a few hundred atoms (similar to molecules). This is the best DFT can currently afford using available high-performance computing (Dorval Cluster) resources. Real plasmonic particles contain tens of thousands of atoms. For Au, one requires at least a thousand atoms for metallicity to manifest. As such, the PDOS plots for Au and Pt are rough approximations of the band structure of Au and Pt nanoparticles. From Figures 6a and b, a sharp decrease of available states in the unoccupied region close to the Fermi level (FL) for Au atoms can be observed in close geometry compared to the far configuration. This reduction of states indicates a reduced

probability of electronic transition within Au. On the other hand, the almost unchanged spectrum for Pt indicates the unaltered transition probability within Pt. However, in the close geometry, the relatively less-affected occupied states for Au and unoccupied states in Pt in the immediate vicinity of FL, clearly shows the likelihood of a high transition rate from Au 3d to Pt 3d states. Hence, molecular orbital and projected density of states analysis strongly corroborate the feasibility of electron transfer from gold to platinum.

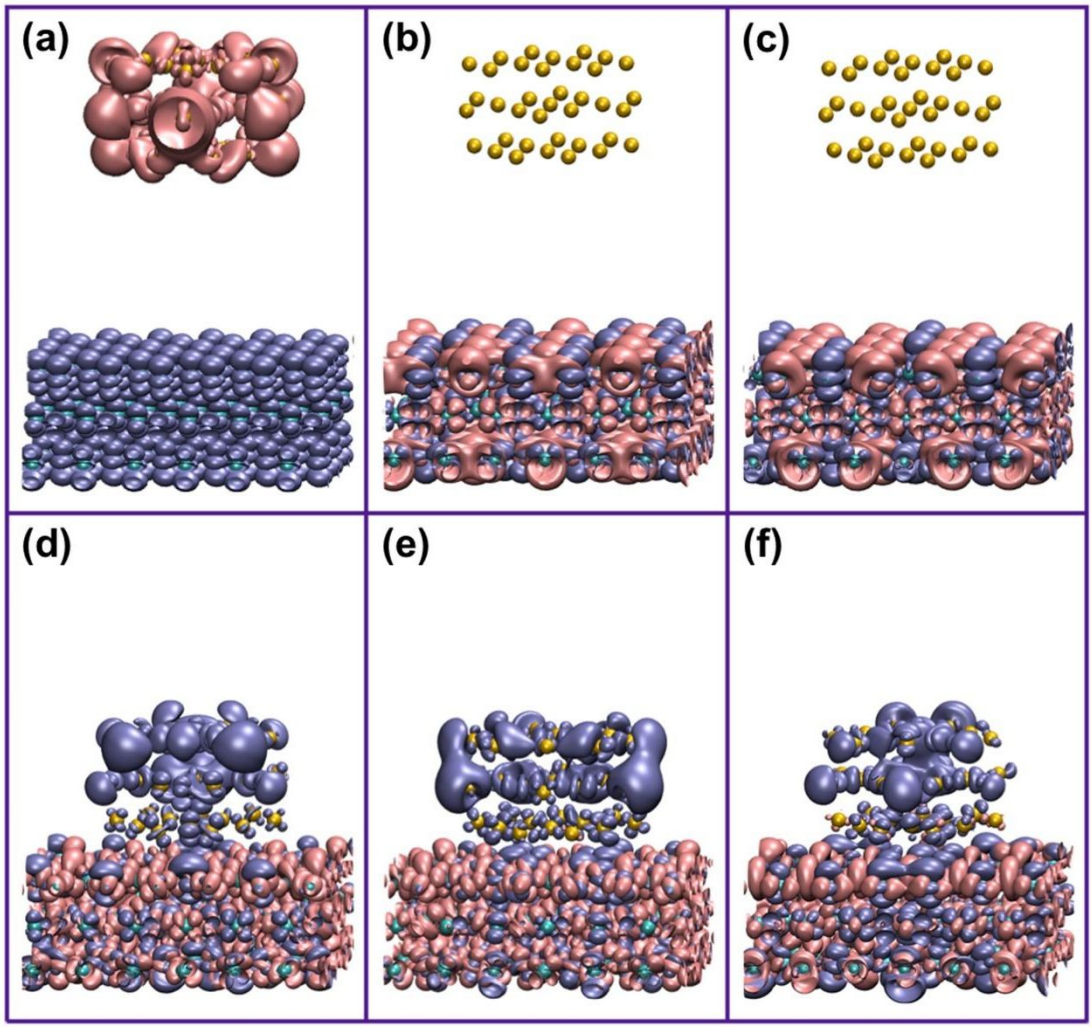

Figure 5. Density functional theory calculated highest occupied molecular orbital (HOMO) and lowest unoccupied molecular orbital (LUMO) of Au@Pt heterosystem are represented by blue and pink colors respectively. (a), (b) and (c) show first, second and third HOMO/LUMO locations respectively, when Au (111) and Pt (111) are far away from each other. (d), (e) and (f) show first, second and third HOMO/LUMO locations respectively, when Au (111) and Pt (111) are in close configuration. Orange and cyan colors are for Au and Pt atoms respectively.

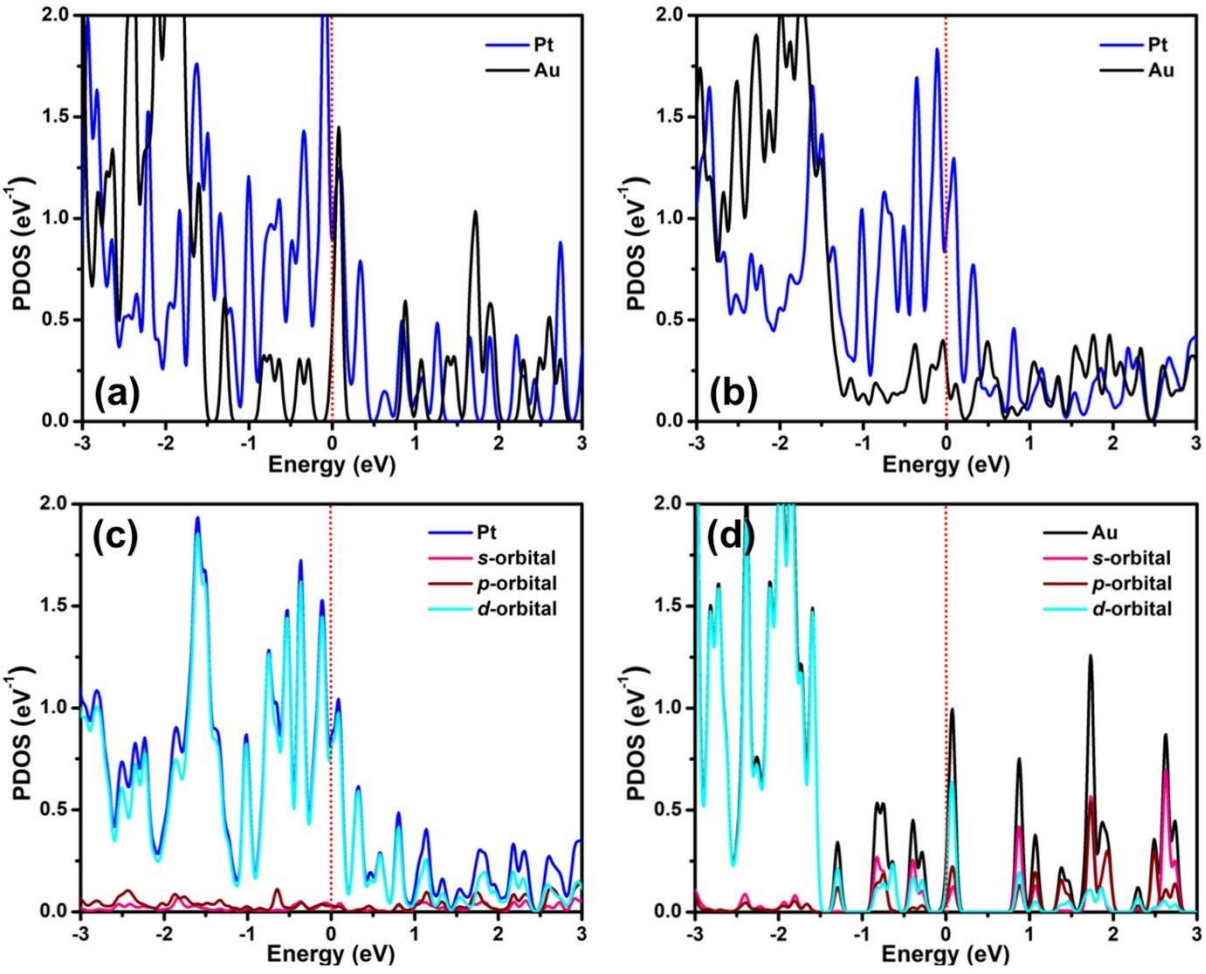

Figure 6. Average projected density of states (PDOS) of Pt and Au systems when (a) Au (111) and Pt (111) are far away from each other and (b) when Au (111) and Pt (111) are in close configuration. Orbital-resolved PDOS of selected (c) Pt and (d) Au atoms at the interfacial region in the far configuration.

2.5 Plasmon-modulated Methylene Blue Dye Degradation

The photocatalytic potential of the Au@Pt core-shell nanoislands was investigated by considering the degradation of methylene blue (MB) dye (see Supporting Information). The characteristic absorption peak of methylene blue at 664 nm was used for monitoring the catalytic degradation process. Absorption spectra of aqueous solutions of MB were tested at different time intervals, following illumination under AM 1.5G light using a Xenon arc lamp solar simulator, and in the presence of the Au@Pt core-shell substrates. At AM 1.5G condition, 1 Sun is defined as equal to 100 mW/cm^2 of irradiance with the standard spectra defined accordingly by the American Society for Testing and Materials (ASTM). The plasmonic substrates were immersed within the dye solutions. As seen in Figure 7a, the main absorption peak of MB demonstrated a gradual decrease with the extension of exposure time (from 60 min in dark to 120 min under AM1.5G), indicating the photocatalytic degradation of the dye. In the absence of the nano-catalyst or in dark conditions, the reaction did not have any progress.

For a quantitative understanding of the degradation process, the change in MB concentration (C) after photodegradation relative to the initial concentration (C_0) of the MB dye was examined. Among the varying ratios of Pt deposition cycles used to fabricate the Au@Pt core-shell nanoislands, Au@Pt samples with a 40 s to 10 s/20 s deposition ratio of Au and Pt demonstrated the greatest degradation efficiencies in correspondence with maximum decrease in intensity in the dye's absorption peak (Figure 7b). These results align with the points that have been made in the prior section on thinner catalytic shells providing better catalytic performance to the bimetallic substrate. These samples performed consistently under AM1.5 G solar illumination as well as illumination under UV filtered light reaching decolorization efficiencies of 24% and 11% (for 40 s – 10 s Au@Pt ratio) and 31% and 17% (for 40 s – 20 s Au@Pt ratio), respectively. Despite these efficiencies being on the lower end, it is important to note that these numbers are dictated for bare bimetallic substrates without the support of a semiconducting scaffold and perform equally if not better than similar substrates fabricated via colloidal techniques. For reference, the bare counterparts involving Au (40 s) and Pt (20 s) demonstrated decolorization efficiencies of 21% and 19%, respectively, under AM 1.5 G solar illumination and efficiencies of 14% and 13%, respectively, under 420 nm UV cut-off filter. The bimetallic counterparts, generally, outperformed

the monometallic systems. The facile means of fabrication involved for these bimetallic hemispherical nanoislands and the modulation of their plasmon resonances provide an open potential for their ease of incorporation with a semiconductor scaffold for greater performance.

The photocatalytic activity of the bimetallic substrates is as follows: Au@Pt (40 s – 20 s ratio) > Au@Pt (40 s – 10 s) > Au@Pt (40 s – 30 s ratio). The photocatalytic activity of the bimetallic substrates can also be described using a pseudo-first-order kinetics model, $-\ln(C/C_0) = kt$, where k is the kinetic rate constant of the degradation process. Figure 7c depicts the kinetics of the MB decomposition for the bimetallic photocatalysts of varying Au and Pt ratios. The measured values of k are 0.00299 (Au@Pt, 40 s – 10 s), 0.00296 (Au@Pt, 40 s – 20 s), and 0.00148 min^{-1} (Au@Pt, 40 s – 30 s). The greatest degradation rate constants are contested between samples where 10 s to 20 s of Pt were deposited.

Investigations into the contribution of primary active species during the photocatalytic degradation process were performed to gain a detailed understanding of the photocatalytic reaction mechanism. Super oxide radicals ($^{\bullet}O_2^-$) and $^{\bullet}OH$ radicals are fundamental to photocatalytic degradation and are activating agents for the oxidation of organic pollutants. Radical trapping experiments using Au@Pt photocatalysts were performed using ethylenediaminetetraacetic acid

(EDTA),isopropyl alcohol (IPA), ammonium dichromate and *p*-benzoquinone as a hole, hydroxyl, electron and superoxide radical scavenger, respectively. To evaluate the photocatalytic performance in the presence of scavengers, 5 mL (10 mM) solutions of scavengers were used. In all four cases, the Au@Pt substrates demonstrated consistently strong dye degradation of the methylene blue dye.[86]

Figure 7d illustrates the effects of the various scavengers in the degradation of MB by the Au@Pt (40 s- 20 s ratio) bimetallic nanoisland photocatalyst. The photodegradation efficiency of MB was significantly lower following the addition of IPA. Ammonium dichromate provides the highest degradation followed by EDTA, *p*-benzoquinone, and finally, IPA. These results suggests that the $^{\bullet}OH$ was the major and $^{\bullet}O_2^-$ the minor radical species responsible for the photocatalytic decomposition of MB over Au@Pt bimetallic nanoisland substrates. The elevated degradation rates in the presence of ammonium dichromate also demonstrate that the plasmonic degradation process is strongly driven by the generation of hot holes.

Our results correlate effectively with observations that thinner shells of Pt provide far better plasmonic performance. The thinner Pt shells help maximize the core plasmon field strength, plasmon-adsorbate coupling, and hot carrier density at the catalytic metal surface. Post 30 s of Pt

deposition, the extensive broadening and damping of the plasmon resonance begins to work against the photocatalytic effectiveness of the substrate. The thicker shells increase the distance and reduce the coupling between the plasmonic core and the catalytic surface resulting in damped plasmon resonances, and as observed in FDTD simulations, dimmer electric field profiles. These results also correlate with what was observed in the UPS spectra. The utilization of thinner Pt shells around gold nanoislands proves to be beneficial as larger shell thicknesses of Pt cause excessive damping leading hot carriers to relax to thermal equilibrium too soon. As the Fermi level of Au@Pt is deeper and more distant from the vacuum level compared to Au, hot holes on the surface of Au@Pt nanoislands will be more strongly oxidizing than hot holes on the surface of bare Au nanoislands. It is well-known that the hot carriers generated in the plasmonic core from the dephasing of the Au LSPR as well as electron intra/interband excitations are generally produced within a fraction of the electron mean free path from the catalytic surface. For Au at 298 K, this equates to a characteristic length of ~ 40 nm.[87] Thus, for thinner Pt shells, one can facilitate the efficient transfer of hot carriers to the adsorbed molecules.[17, 35, 88-90] Due to this, bimetallic substrates with lower Pt deposition rates provides efficient photo-absorption and charge/energy delivery to catalytic sites on the surface.

It is also important to note that the average electric field enhancement on the surface of an isolated Au nanoparticle is larger for smaller sizes.[33] These intense local fields can effectively help trigger chemical reactions on the surface of the substrate. For thicker shells, the effective charge-energy transfer will be weakened due to weaker plasmon-surface coupling as the hot carriers will consistently lose energy as they move from the core to the shell surface. It is observed that ~ 20-30% of hot carriers scatter and lose their excess energy by transiting a 2 nm thick Pt shell.[91-94] Post 30 s of Pt deposition, the existence of a thicker shell maximizes these losses. These losses could be attributed to faster carrier cooling in Pt due to stronger e-p coupling or alternatively rapid e-e transfer from the Au core to the Pt shell at a < 1 ps timescale.[1, 95] For thicker Pt shells, these effects collectively manifest in the form of the strong interfacial damping and broadening of the Au LSPR further debilitating visible-light photocatalytic processes.

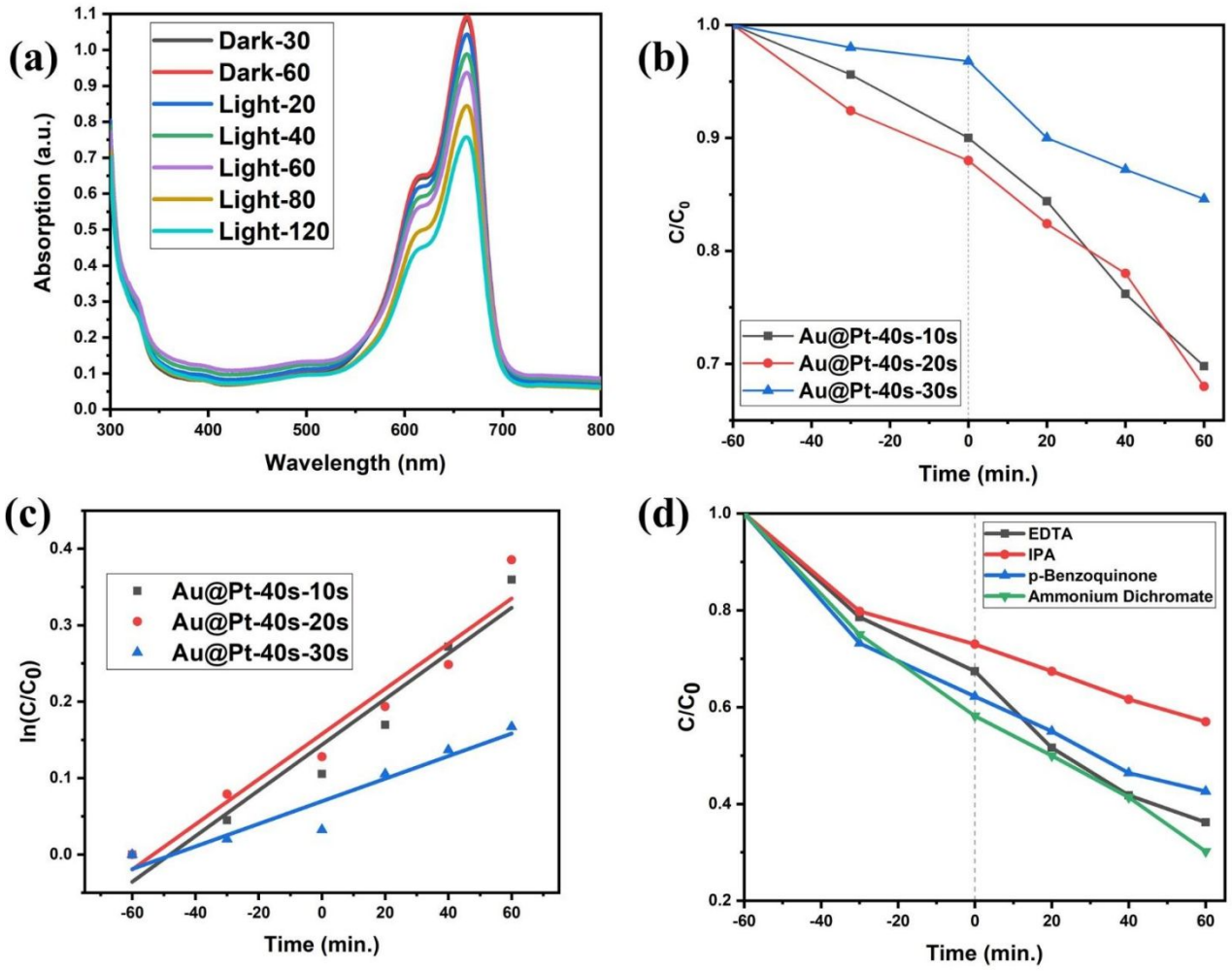

Figure 7. (a) Photodegradation of MB under solar light illumination in the presence Au@Pt core-shell hemispherical nanoisland photocatalyst. (b) Photodegradation of MB for Au@Pt core-shell photocatalyst for varying Pt deposition durations. (c) Kinetic rates study of MB degradation for Au@Pt samples with varying Pt deposition durations. (d) Photodegradation of MB degradation for Au@Pt samples in the presence of electron and hole scavengers.

The strong damping of the Au LSPR and the red-shifting of its resonance wavelength offer the contrary possibility that Pt electrons also participate in the collective charge density oscillations.[72]

Essentially, the Au core acts as a plasmonic antenna for light harvesting. The resultant energy and generation of hot carriers of the LSPR is delivered to the catalytic Pt shell. By engineering the catalytic shell one can modulate the flow of electromagnetic energy from the plasmonic core to the catalytic surface though it is far from clear how this happens. Raman thermometric studies of the MB adsorbate – bimetallic substrate system may offer some basic insights into the process.

2.6 Raman thermometry studies

Raman thermometry studies provide a basic tool in studying the dynamics of plasmonic charge transfer of hot carriers on bimetallic substrates and has been investigated by Boerigter et al.[46] Wavelength-dependent Stokes and anti-Stokes surface-enhanced Raman spectroscopy (SERS) of methylene blue molecules chemisorbed on Au@Pt core-shell nanoisland substrates structures has been used to probe plasmon induced direct charge transfer (see Supporting Information). The Stokes Raman signal is indicative of the rate of transition of a molecule excited from its ground state to its first vibration state. The reverse-transition is indicated by the anti-Stokes Raman signal.[96] As such, by monitoring the vibrational temperature of the plasmonic substrate and the attached adsorbate simultaneously upon resonant illumination, one can discern the flow of charge

carriers from the metal nanoparticle to the adsorbed molecules via plasmon induced hot carrier injection.[82]

Stokes and anti-Stokes scattering signals were measured for the most consistent of our bimetallic Au@Pt core-shell nanoisland substrates. These substrates involved a 40 s Au to 20 s Pt deposition ratio. Lattice temperatures were calculated and the corresponding Stokes and anti-Stokes Raman spectrum of the bimetallic composite upon illumination by a 532 nm laser is shown in (Figure 8). We found that under 532 nm illumination, due to weak anti-Stokes signals, we were only able to confidently measure the temperatures of the 328 cm^{-1}, 442 cm^{-1} and 491 cm^{-1} modes. (Table 2)

Raman Mode (cm^{-1})	Temperature (K)
328	397.81
442	332.38
491	397.05

Table 2. Raman temperatures for corresponding Raman modes.

The rise in temperature though seemingly small is comparable to those generated involving bimetallic substrates with an MB adsorbate under 532 nm illumination.[46, 82] The low temperatures

can also be attributed to the strong damping, as observed from the broadened linewidths of the LSPR spectra in (Figure 1b), in the Au@Pt bimetallic system when compared to monometallic Au nanoislands. As seen in the work of Boerigter et al.,[46] illumination closer to the red-shifted resonance value of the Au@Pt bimetallic substrate may provide greater anti-Stokes signal intensities. The temperature rise is still indicative of an elevated vibrational population in the adsorbate-plasmon system and is a signature of plasmon generated hot carrier injection from the bimetallic substrate to the surface. This is also particularly impressive considering that Au in general does not provide temperature enhancement for MB adsorbates while its counterpart in Ag does a much better job, furthering the potential of Au@Pt as a standalone plasmonic substrate.

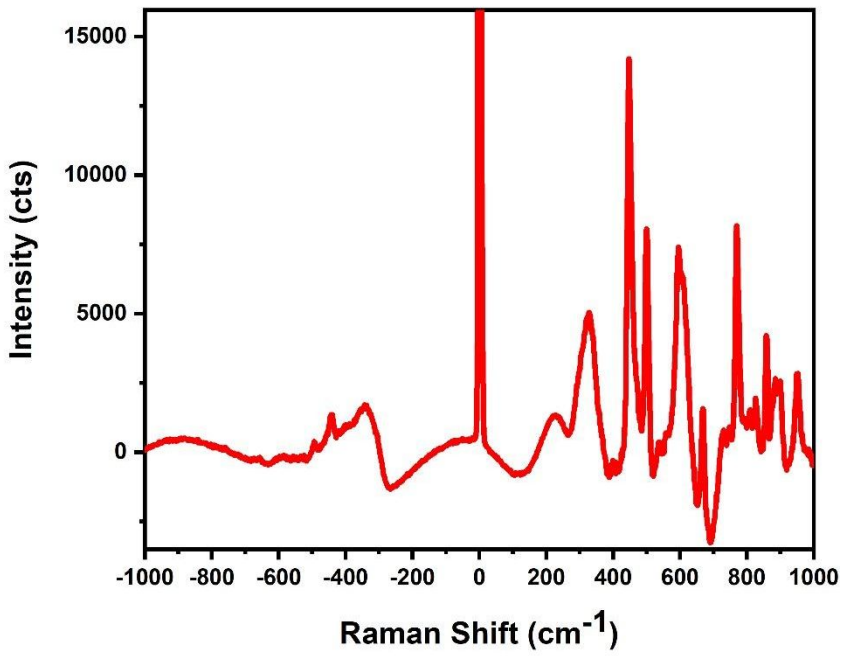

Figure 8. Raman thermometry Stokes and anti-Stokes spectra of MB on Au@Pt core-shell substrate.

Conclusion

Au@Pt core-shell nanoislands on glass were fabricated using a combination of magnetron sputtering and thermal annealing in a process that provides greater consistency compared to wet-chemical or colloidal synthetic techniques. The addition of Pt shells of varying thicknesses provided for the modulation of the plasmonic response of the bimetallic composite while offering insights into the photocatalytic potential of the bimetallic substrates in the absence of a semiconductor support via methylene blue dye degradation. Au@Pt NPs exhibited a lattice strain of ~0.2%. The corresponding results suggested the necessity and importance of shell engineering to provide for efficient plasmon-mediated chemical conversion with thinner Pt shells providing greater scope for dye degradation as opposed to thicker shells. FDTD simulations provided fundamental insights into the crucial influence of morphology and the advantage of inter-island channels and gaps to amplify the plasmonic activity of the bimetallic substrates. The addition of the Pt film provides for a general increase in absorption intensity as well as a catalytic surface for adsorption and surface insulation allowing for sample stability. Pt loading of the Au nanoislands

progressively broadens the Au LSPR and is proof of strong electronic coupling between the Au LSPR and the catalytic metal at the substrate surface. The resulting resonance is slightly red-shifted but indicates that the LSPR effect is largely delegated by the plasmonic Au core. The integration of both metals creates a broadband optical resonance which is a prerequisite for many applications in photocatalysis. Altogether, our study demonstrates a facile means to fabricate Au@Pt bimetallic substrates that are effective as standalone plasmonic catalysts, and whose potential can be improved via shell engineering of the Pt surface. Raman thermometric studies confirm the existence of plasmon generated hot carrier injection that facilitates dye degradation where the LSPR of the Au core dephases via the generation of hot carriers expelled into the Pt shell which are subsequently injected into the dye molecules at the surface.

Acknowledgements

This research was funded by the Natural Sciences and Engineering Research Council of Canada (NSERC), Future Energy Systems (FES), and the National Research Council – National Institute for Nanotechnology (NRC-NINT).

References

1. C. Engelbrekt, K. T. Crampton, D. A. Fishman, M. Law and V. A. Apkarian, *ACS Nano*, 2020, **14**, 5061-5074.
2. A. P. Manuel, A. Kirkey, N. Mahdi and K. Shankar, *J. Mater. Chem. C*, 2019, **7**, 1821-1853.
3. S. Linic, P. Christopher and D. B. Ingram, *Nat. Mater.*, 2011, **10**, 911-921.
4. S. Zeng, E. Vahidzadeh, C. G. VanEssen, P. Kar, R. Kisslinger, A. Goswami, Y. Zhang, N. Mandi, S. Riddell, A. E. Kobryn, S. Gusarov, P. Kumar and K. Shankar, *Applied Catalysis B-Environmental*, 2020, **267**.
5. F. Michael, *Philosophical Transactions of the Royal Society of London*, 1857, **147**, 145-181.
6. U. Kreibig and M. Vollmer, *Optical properties of metal clusters*, Springer, 1995.
7. E. J. Zeman and G. C. Schatz, *The Journal of Physical Chemistry*, 1987, **91**, 634-643.
8. G. V. Hartland, *The Journal of Physical Chemistry Letters*, 2014, **5**, 1583-1584.
9. G. V. Hartland, *Chem. Rev.*, 2011, **111**, 3858-3887.
10. A. P. Manuel and K. Shankar, *Nanomaterials*, 2021, **11**.
11. K. Sytwu, M. Vadai and J. A. Dionne, *Advances in Physics: X*, 2019, **4**, 1619480.
12. U. Aslam, V. G. Rao, S. Chavez and S. Linic, *Nature Catalysis*, 2018, **1**, 656-665.
13. C. Zhan, X.-J. Chen, J. Yi, J.-F. Li, D.-Y. Wu and Z.-Q. Tian, *Nat. Rev. Chem.*, 2018, **2**, 216-230.
14. S. Linic, U. Aslam, C. Boerigter and M. Morabito, *Nat. Mater.*, 2015, **14**, 567-576.
15. S. Sim, A. Beierle, P. Mantos, S. McCrory, R. P. Prasankumar and S. Chowdhury, *Nanoscale*, 2020, **12**, 10284-10291.
16. S. Mukherjee, F. Libisch, N. Large, O. Neumann, L. V. Brown, J. Cheng, J. B. Lassiter, E. A. Carter, P. Nordlander and N. J. Halas, *Nano Lett.*, 2013, **13**, 240-247.
17. H. Huang, L. Zhang, Z. Lv, R. Long, C. Zhang, Y. Lin, K. Wei, C. Wang, L. Chen, Z.-Y. Li, Q. Zhang, Y. Luo and Y. Xiong, *J. Am. Chem. Soc.*, 2016, **138**, 6822-6828.
18. R. Long, Z. Rao, K. Mao, Y. Li, C. Zhang, Q. Liu, C. Wang, Z.-Y. Li, X. Wu and Y. Xiong, *Angew. Chem., Int. Ed.*, 2015, **54**, 2425-2430.
19. F. Wang, C. Li, H. Chen, R. Jiang, L.-D. Sun, Q. Li, J. Wang, J. C. Yu and C.-H. Yan, *J. Am. Chem. Soc.*, 2013, **135**, 5588-5601.

20. J. R. Adleman, D. A. Boyd, D. G. Goodwin and D. Psaltis, *Nano Lett.*, 2009, **9**, 4417-4423.
21. L. Guo, Q. Sun, K. Marcus, Y. Hao, J. Deng, K. Bi and Y. Yang, *J. Mater. Chem. A*, 2018, **6**, 22005-22012.
22. J. M. Walker, L. Gou, S. Bhattacharyya, S. E. Lindahl and J. M. Zaleski, *Chem. Mater.*, 2011, **23**, 5275-5281.
23. K. M. Haas and B. J. Lear, *Chemical Science*, 2015, **6**, 6462-6467.
24. T. P. Araujo, J. Quiroz, E. C. M. Barbosa and P. H. C. Camargo, *Curr. Opin. Colloid Interface Sci.*, 2019, **39**, 110-122.
25. E. Vahidzadeh, S. Zeng, A. P. Manuel, S. Riddell, P. Kumar, K. M. Alam and K. Shankar, *ACS Appl. Mater. Inter.*, 2021, **13**, 7248-7258.
26. V. Amendola, R. Pilot, M. Frasconi, O. M. Maragò and M. A. Iatì, *J. Phys.: Condens. Matter*, 2017, **29**, 203002.
27. K. L. Kelly, E. Coronado, L. L. Zhao and G. C. Schatz, *J. Phys. Chem. B*, 2003, **107**, 668-677.
28. D. F. Swearer, H. Zhao, L. Zhou, C. Zhang, H. Robatjazi, J. M. P. Martirez, C. M. Krauter, S. Yazdi, M. J. McClain, E. Ringe, E. A. Carter, P. Nordlander and N. J. Halas, *Proceedings of the National Academy of Sciences*, 2016, **113**, 8916.
29. C. Zhang, H. Zhao, L. Zhou, A. E. Schlather, L. Dong, M. J. McClain, D. F. Swearer, P. Nordlander and N. J. Halas, *Nano Lett.*, 2016, **16**, 6677-6682.
30. A. Joplin, S. A. Hosseini Jebeli, E. Sung, N. Diemler, P. J. Straney, M. Yorulmaz, W.-S. Chang, J. E. Millstone and S. Link, *ACS Nano*, 2017, **11**, 12346-12357.
31. L. Ranno, S. D. Forno and J. Lischner, *npj Computational Materials*, 2018, **4**, 31.
32. C. Zhang, B.-Q. Chen, Z.-Y. Li, Y. Xia and Y.-G. Chen, *J. Phys. Chem. C*, 2015, **119**, 16836-16845.
33. S. Chavez, U. Aslam and S. Linic, *ACS Energy Letters*, 2018, **3**, 1590-1596.
34. M. G. Blaber, M. D. Arnold and M. J. Ford, *J. Phys.: Condens. Matter*, 2010, **22**, 143201.
35. Y. Zhang, S. He, W. Guo, Y. Hu, J. Huang, J. R. Mulcahy and W. D. Wei, *Chem. Rev.*, 2018, **118**, 2927-2954.
36. W. Ye, H. Kou, Q. Liu, J. Yan, F. Zhou and C. Wang, *Int. J. Hydrogen Energy*, 2012, **37**, 4088-4097.

37. S.-C. Lin, C.-S. Hsu, S.-Y. Chiu, T.-Y. Liao and H. M. Chen, *J. Am. Chem. Soc.*, 2017, **139**, 2224-2233.
38. U. Aslam, S. Chavez and S. Linic, *Nat. Nanotechnol.*, 2017, **12**, 1000-1005.
39. Z. Zheng, T. Tachikawa and T. Majima, *J. Am. Chem. Soc.*, 2014, **136**, 6870-6873.
40. J. Guo, Y. Zhang, L. Shi, Y. Zhu, M. F. Mideksa, K. Hou, W. Zhao, D. Wang, M. Zhao, X. Zhang, J. Lv, J. Zhang, X. Wang and Z. Tang, *J. Am. Chem. Soc.*, 2017, **139**, 17964-17972.
41. L. Zhou, D. F. Swearer, C. Zhang, H. Robatjazi, H. Zhao, L. Henderson, L. Dong, P. Christopher, E. A. Carter, P. Nordlander and N. J. Halas, *Science*, 2018, **362**, 69.
42. H. F. Zarick, A. Boulesbaa, A. A. Puretzky, E. M. Talbert, Z. R. DeBra, N. Soetan, D. B. Geohegan and R. Bardhan, *Nanoscale*, 2017, **9**, 1475-1483.
43. Z. Yu, Y. Gao, L. Sang and L. Lei, *Catalysis Science & Technology*, 2021, **11**, 6529-6536.
44. M. J. Weber, A. J. M. Mackus, M. A. Verheijen, C. van der Marel and W. M. M. Kessels, *Chem. Mater.*, 2012, **24**, 2973-2977.
45. A. P. Manuel, P. Barya, S. Riddell, S. Zeng, K. M. Alam and K. Shankar, *Nanotechnology*, 2020, **31**, 365301.
46. C. Boerigter, U. Aslam and S. Linic, *ACS Nano*, 2016, **10**, 6108-6115.
47. K. Wu, J. Chen, J. R. McBride and T. Lian, *Science*, 2015, **349**, 632.
48. N. R. Agarwal, P. M. Ossi and S. Trusso, *Appl. Surf. Sci.*, 2019, **466**, 19-27.
49. M. Altomare, N. T. Nguyen and P. Schmuki, *Chemical Science*, 2016, **7**, 6865-6886.
50. S. Yang, F. Xu, S. Ostendorp, G. Wilde, H. Zhao and Y. Lei, *Advanced Functional Materials*, 2011, **21**, 2446-2455.
51. M. Kracker, W. Wisniewski and C. Rüssel, *RSC Advances*, 2014, **4**, 48135-48143.
52. C. M. Müller, F. C. F. Mornaghini and R. Spolenak, *Nanotechnology*, 2008, **19**, 485306.
53. D. L. Smith, *Journal*, 1995.
54. D. Wang, X. Cui, Q. Xiao, Y. Hu, Z. Wang, Y. M. Yiu and T. K. Sham, *AIP Advances*, 2018, **8**, 065210.
55. M. Ma, H. A. Hansen, M. Valenti, Z. Wang, A. Cao, M. Dong and W. A. Smith, *Nano Energy*, 2017, **42**, 51-57.
56. C. Tan, Y. Sun, J. Zheng, D. Wang, Z. Li, H. Zeng, J. Guo, L. Jing and L. Jiang, *Scientific Reports*, 2017, **7**, 6347.

57. B. G. C. Bond, *Platinum Metals Review*, 2007, **51**, 63-68.
58. Y. Wang and M. Hou, *The Journal of Physical Chemistry C*, 2012, **116**, 10814-10818.
59. S. Farsinezhad, H. Sharma and K. Shankar, *Phys. Chem. Chem. Phys.*, 2015, **17**, 29723-29733.
60. G. Geng, P. Chen, B. Guan, Y. Liu, C. Yang, N. Wang and M. Liu, *RSC Adv.*, 2017, **7**, 51838-51846.
61. C. A. Rodríguez-Proenza, J. P. Palomares-Báez, M. A. Chávez-Rojo, A. F. García-Ruiz, C. L. Azanza-Ricardo, A. Santoveña-Uribe, G. Luna-Bárcenas, J. L. Rodríguez-López and R. Esparza, *Materials*, 2018, **11**.
62. N. Goubet, I. Tempra, J. Yang, G. Soavi, D. Polli, G. Cerullo and M. P. Pileni, *Nanoscale*, 2015, **7**, 3237-3246.
63. Y. U. Staechelin, D. Hoeing, F. Schulz and H. Lange, *ACS Photonics*, 2021, **8**, 752-757.
64. C. A. García-Negrete, B. R. Knappett, F. P. Schmidt, T. C. Rojas, A. E. H. Wheatley, F. Hofer and A. Fernández, *RSC Advances*, 2015, **5**, 55262-55268.
65. J. W. J. P. Clarkson, and P. M. Fauchet, *Optical Materials Express*, 2011, **1**, 970-979.
66. B. E. Sundquist, *Acta Metallurgica*, 1964, **12**, 67-86.
67. W. Haiss, N. T. K. Thanh, J. Aveyard and D. G. Fernig, *Anal. Chem.*, 2007, **79**, 4215-4221.
68. M.-M. Jiang, H.-Y. Chen, B.-H. Li, K.-W. Liu, C.-X. Shan and D.-Z. Shen, *J. Mater. Chem. C*, 2014, **2**, 56-63.
69. T. Klar, M. Perner, S. Grosse, G. von Plessen, W. Spirkl and J. Feldmann, *Physical Review Letters*, 1998, **80**, 4249-4252.
70. S. Farsinezhad, S. P. Banerjee, B. Bangalore Rajeeva, B. D. Wiltshire, H. Sharma, A. Sura, A. Mohammadpour, P. Kar, R. Fedosejevs and K. Shankar, *ACS Applied Materials & Interfaces*, 2017, **9**, 740-749.
71. L. Bazán-Díaz, R. Mendoza-Cruz, C.-K. Liao and M. A. Mahmoud, *J. Phys. Chem. C*, 2019, **123**, 30509-30518.
72. D.-C. Marinica, J. Aizpurua and A. G. Borisov, *Opt. Express*, 2016, **24**, 23941-23956.
73. S. Griffin, N. P. Montoni, G. Li, P. J. Straney, J. E. Millstone, D. J. Masiello and J. P. Camden, *The Journal of Physical Chemistry Letters*, 2016, **7**, 3825-3832.
74. J.-F. Li, Z.-L. Yang, B. Ren, G.-K. Liu, P.-P. Fang, Y.-X. Jiang, D.-Y. Wu and Z.-Q. Tian, *Langmuir*, 2006, **22**, 10372-10379.

75. C. A. Murray, *Journal of Electron Spectroscopy and Related Phenomena*, 1983, **29**, 371-382.
76. S. Zou and M. J. Weaver, *Analytical Chemistry*, 1998, **70**, 2387-2395.
77. K. Zhang, Y. Xiang, X. Wu, L. Feng, W. He, J. Liu, W. Zhou and S. Xie, *Langmuir*, 2009, **25**, 1162-1168.
78. E. Prodan, C. Radloff, N. J. Halas and P. Nordlander, *Science*, 2003, **302**, 419-422.
79. P. Nordlander, C. Oubre, E. Prodan, K. Li and M. I. Stockman, *Nano Lett.*, 2004, **4**, 899-903.
80. B. Barman, H. Dhasmana, A. Verma, A. Kumar, D. N. Singh and V. K. Jain, *Energy & Environment*, 2018, **29**, 358-371.
81. R. Long, Y. Li, L. Song and Y. Xiong, *Small*, 2015, **11**, 3873-3889.
82. C. Boerigter, R. Campana, M. Morabito and S. Linic, *Nat. Commun.*, 2016, **7**, 10545.
83. Z. Zhang, U. Gernert, R. F. Gerhardt, E.-M. Höhn, D. Belder and J. Kneipp, *ACS Catal.*, 2018, **8**, 2443-2449.
84. R. Sundararaman, P. Narang, A. S. Jermyn, W. A. Goddard Iii and H. A. Atwater, *Nature Communications*, 2014, **5**, 5788.
85. O. A. Douglas-Gallardo, M. Berdakin, T. Frauenheim and C. G. Sánchez, *Nanoscale*, 2019, **11**, 8604-8615.
86. A. Zielińska-Jurek, *Journal of Nanomaterials*, 2014, **2014**, 208920.
87. R. H. Doremus, *The Journal of Chemical Physics*, 1964, **40**, 2389-2396.
88. G. V. Hartland, L. V. Besteiro, P. Johns and A. O. Govorov, *ACS Energy Letters*, 2017, **2**, 1641-1653.
89. L. V. Besteiro and A. O. Govorov, *The Journal of Physical Chemistry C*, 2016, **120**, 19329-19339.
90. A. M. Brown, R. Sundararaman, P. Narang, A. M. Schwartzberg, W. A. Goddard and H. A. Atwater, *Physical Review Letters*, 2017, **118**, 087401.
91. J. Patterson, *The London, Edinburgh, and Dublin Philosophical Magazine and Journal of Science*, 1902, **4**, 652-678.
92. G. Fischer, H. Hoffmann and J. Vancea, *Physical Review B*, 1980, **22**, 6065-6073.
93. S. Dutta, K. Sankaran, K. Moors, G. Pourtois, S. Van Elshocht, J. Bömmels, W. Vandervorst, Z. Tőkei and C. Adelmann, *Journal of Applied Physics*, 2017, **122**, 025107.
94. D. Gall, *Journal of Applied Physics*, 2020, **127**, 050901.

95. J. H. Hodak, A. Henglein and G. V. Hartland, *The Journal of Chemical Physics*, 2001, **114**, 2760-2765.

96. R. C. Maher, C. M. Galloway, E. C. Le Ru, L. F. Cohen and P. G. Etchegoin, *Chemical Society Reviews*, 2008, **37**, 965-979.